InSAR Phase Unwrapping Error Correction for Rapid Repeat Measurements of Water Level Change in Wetlands

Talib Oliver-Cabrera, Cathleen E. Jones, *Member, IEEE* , Zhang Yunjun, and Marc Simard

***Abstract*— Here, we present an enhanced algorithm to correct interferometric synthetic aperture radar (InSAR) phase unwrapping errors by incorporating iterative spatial bridging between islands and phase closure among interferograms. We use rapid repeat airborne synthetic aperture radar acquisitions from NASA's airborne uninhabited aerial vehicle synthetic aperture radar (UAVSAR) instrument to estimate short-term changes in water level within coastal wetlands from a stack of consecutive interferograms acquired with very short temporal separation (∼30 min). The algorithm is applied to six consecutive UAVSAR images collected in tidal wetlands of the Wax Lake Delta, Louisiana, USA. Validation of our water level change retrievals with *in situ* field observations was conclusive with high correlation and an RMSE generally smaller than 3 cm. Comparison of our algorithm with other phase unwrapping error correction methods shows significant improvement (30%–35% increase in the number of correctly unwrapped pixels) when applied to rapid changes in water level. The set of corrections presented in this work enables measurement of water level change in deltas and other areas where tides drive highly dynamic flooding of inland vegetated areas. Although demonstrated for water level change, the method is applicable to other InSAR datasets with large spatial gradients or observed discontinuities between coherent but spatially isolated areas.**

***Index Terms*— Interferometric synthetic aperture radar (InSAR), phase unwrapping correction, uninhabited aerial vehicle synthetic aperture radar (UAVSAR), water level change, wetlands.**

I. Introduction

WETLAND environments are very dynamic ecosystems for which hydrological monitoring is essential to better understand the complex interactions between vegetation, water flow, nutrients, and sediment transport. Tide gauge measurements are commonly used for this purpose, providing data at a very high temporal sampling [1]. However, the coverage is sparse, usually located at the edges of wetlands to simplify logistics, making it difficult to observe water-flow patterns throughout the wetlands. Interferometric synthetic aperture radar (InSAR) is a powerful remote sensing and geodetic technique used to measure surface deformation with high precision. It is widely used to observe geophysical and environmental phenomena [2]–[4]. In wetland environments, InSAR can provide spatially extensive water level change measurements through the double-bounce scattering of the radar pulses with the water surface and emergent vegetation [5]–[7]. The InSAR technique has been used as a monitoring tool to observe and characterize water level change and patterns across wetlands [8]–[10], spatially complementing tide gauge information.

Even though wetland InSAR has shown promising results, it is still limited. The technique is dependent on the double-bounce scattering provided by wetland emergent vegetation [11]. Thus, the approach is highly sensitive to surface changes in water or vegetation that lead to loss of interferometric coherence. As a result, most wetland InSAR application is limited to short temporal baseline interferograms, typically less than a few weeks, and to regions away from the coast where the tide induces rapid (∼hourly) changes in water level. Perhaps, the most important step in the process of retrieving water level change using InSAR is phase unwrapping. In an interferogram, the component of surface displacement in the line-of-sight direction is related to the interferometric phase, $\Delta\phi$, which has values in the range $[0, 2\pi)$, where 2π corresponds to displacement equal to half the radar wavelength, λ, due to the two-way travel of the microwaves from the antenna to the surface and back. Displacements of greater magnitude "wrap" back onto this range, so it is necessary to quantify the phase ambiguity, i.e., the number of 2π cycles, to be able to accurately derive the total displacement. This process is known as phase unwrapping. The number of cycles, n, is determined for every pixel in an interferogram from the observed spatial patterns of phase ($\Delta\phi$) and assuming a spatially continuous InSAR unwrapped phase, $n2\pi + \Delta\phi$, map. A continuous map of the unwrapped phase can only be obtained if adjacent pixels are coherent (i.e., InSAR coherence is high). InSAR phase unwrapping in coastal wetlands is challenging because: 1) the landscape is naturally separated into islands, so there may not be a continuous coherent path between islands that would enable relating the phase wrap on one island to that on adjacent islands; 2) tidal dynamics often drive rapid and different

Manuscript received June 16, 2021; revised August 9, 2021; accepted August 25, 2021. Date of publication September 15, 2021; date of current version January 26, 2022. The work of Talib Oliver-Cabrera, Cathleen E. Jones, and Marc Simard was supported by the National Aeronautics and Space Administration's (NASA) Delta-X mission, which is funded by the Science Mission Directorate's Earth Science Division through the Earth Venture Suborbital-3 Program NNH17ZDA001N-EVS3. *(Corresponding author: Talib Oliver-Cabrera.)*

Talib Oliver-Cabrera, Cathleen E. Jones, and Marc Simard are with the Jet Propulsion Laboratory, California Institute of Technology, Pasadena, CA 91109 USA (e-mail: talib.oliver.cabrera@jpl.nasa.gov).

Zhang Yunjun is with the Seismological Laboratory, California Institute of Technology, Pasadena, CA 91109 USA.

This article has supplementary downloadable material available at https://doi.org/10.1109/TGRS.2021.3108751, provided by the authors.

Digital Object Identifier 10.1109/TGRS.2021.3108751

changes in water levels across the landscape components, resulting in high phase gradients; and 3) riverine flooding can overtop vegetation, thereby replacing double-bounce scattering with scattering from open water, which does not maintain coherence. These phenomena cause temporal decorrelation and high phase gradients, resulting in incorrect determination of the numbers of phase cycles (2π) during phase unwrapping.

Different methods to mitigate this problem have been developed. Biggs *et al.* [12], Yunjun *et al.* [13], Pepe *et al.* [14], Benoit *et al.* [15], and Ma *et al.* [16] exploit the interferometric triplet inconsistencies to evaluate errors among unwrapped interferograms. Ma *et al.* [16] and Manunta and Muhammad [17] take advantage of compressed sensing (CS) theory to solve for redundant networks of interferograms, while Yunjun *et al.* [13] and Benoit *et al.* [15] use a combined approach of corrections in the space and time domains. Alternatively, other methods exploit redundant measurements, as well as spatial and time relationships, among interferograms to improve the unwrapping task directly, thus minimizing the presence of unwrapping errors [18].

This study presents an enhanced phase unwrapping correction algorithm to improve water level change retrieval. The algorithm incorporates spatial bridging between islands and imposes phase closure among interferograms (e.g., [13]). An iterative strategy is implemented to correct interferograms with the shortest temporal baseline first and then adding interferograms with longer temporal baselines, increasing the redundancy of the interferometric estimates through each iteration. To test the algorithm, we take advantage of the highly coherent rapid repeat-pass SAR acquisitions from uninhabited aerial vehicle synthetic aperture radar (UAVSAR), using data acquired in 2016 over coastal wetlands of Louisiana, USA, encompassing the coastal stretch of the Atchafalaya Basin. While spaceborne sensors can acquire a wider overview of coastal Louisiana, their long temporal baselines provide coherent InSAR in swamp regions but not in herbaceous marshes (e.g., [10], [19], and [20]). The Mississippi River Delta (MRD) region is generally known for rapid land loss [21], and the Atchafalaya basin is the only part of the MRD floodplain gaining land [22], [23]. Two small deltas can be found within the Atchafalaya Basin, the Wax Lake Delta to the west, and the Atchafalaya River Delta to the east (see Fig. 1). Both deltas are comprised of many wetland islands, most under 5-km long. We focus our analysis on the deltaic region (red rectangle in Fig. 1) because it is within those regions that most of the wetland islands and phase gradients are observed, and thus, where phase unwrapping is more difficult.

II. Dataset

The dataset consists of a coregistered stack of six single-look complex (SLC) UAVSAR images for flight line ID gulfco_12011, covering the Wax Lake and Atchafalaya River deltas (see Fig. 1). The acquisitions were taken approximately 30 min apart on October 17, 2016, during the rising-to-high tide. UAVSAR is an L-band (23.8-cm wavelength) instrument deployed on a NASA Gulfstream III aircraft. It acquires quad polarization images, with a resolution of 0.6 m in azimuth (along track direction) by 1.7 m in slant range. UAVSAR data are publicly available and can be found at http://uavsar.jpl.nasa.gov. For this work, we used only the HH-polarization acquisitions since that mode is more sensitive to double-bounce backscattering and, hence, better for measuring water level changes [19]. The UAVSAR data product is calibrated and, therefore, provides a set of six HH-polarization elements of the complex scattering matrix, S, i.e.,

$$S_i, \quad i = 0, \ldots, m-1 \tag{1}$$

where $m = 6$. A multilooking factor of 12 pixels in azimuth and 3 in slant range was applied to the interferograms generated from S_i. Phase unwrapping was performed on these products without additional spatial filtering. Hourly water level measurements from the Coastwide Reference Monitoring System (CRMS) stations were used to validate the InSAR observations. CRMS data are freely available from https://www.lacoast.gov/CRMS.

III. Methodology

We use pairs of rapid-repeat pass SAR acquisitions acquired by UAVSAR to form sets of interferograms employing the InSAR Scientific Computing Environment (ISCE) (Rosen *et al.* [24]). The interferogram, calculated as

$$S_i S_j^* = A_{ij} e^{-\imath(\varphi_j - \varphi_i)} = A_{ij} e^{-\imath \Delta\varphi_{i,j}} \tag{2}$$

provides the interferometric phase, $\Delta\varphi_{i,j}$, for the pair of acquisitions i and j. The interferometric phase obtained from the interferogram, $\Delta\varphi^w$, has the 2π ambiguity mentioned above, and the superscript "w" is added to make that clear. The interferometric phase is related to the change in distance to the surface in the line-of-sight direction, Δl, and the radar wavelength, λ, through the equation

$$\Delta l = \frac{\lambda}{4\pi}\left(\Delta\varphi^w + n(2\pi)\right) = \frac{\lambda}{4\pi}\left(\Delta\varphi^u\right) \tag{3}$$

where a phase unwrapping algorithm is applied to determine the number of cycles, n, to obtain the unwrapped phase, $\Delta\varphi^u$. Phase changes can be used to measure water level changes, Δw, within flooded wetlands where emergent vegetation is present through the relationship

$$\Delta w = -\frac{\lambda}{4\pi}\frac{\Delta\varphi^u}{\cos\theta} \tag{4}$$

where θ is the incidence angle of the radar pulses. The negative sign is added to make explicit the UAVSAR convention that a positive change in phase corresponds to an increase in distance between the antenna and the ground. This relationship is used to convert the observed change in line-of-sight distance to the vertical change in water level.

For this work, three sets of interferograms are generated to obtain the phase changes, $\Delta\varphi_{ij}^w$, between different acquisitions. The first set is formed between the nearest neighbor (NN) interferograms with phases

$$\Delta\varphi_{\mathrm{NN}}^w \equiv \left\{\Delta\varphi_{i,i+1}^w \forall i \in (0, \ldots, m-1)\right\}. \tag{5}$$

This is the set of interferograms with the shortest temporal baselines, ~30 min in the case of our study. Similarly, NN + 1 interferograms with phases

$$\Delta\varphi_{\mathrm{NN}+1}^w \equiv \left\{\Delta\varphi_{i,i+2}^w \forall i \in (0, \ldots, m-2)\right\} \tag{6}$$

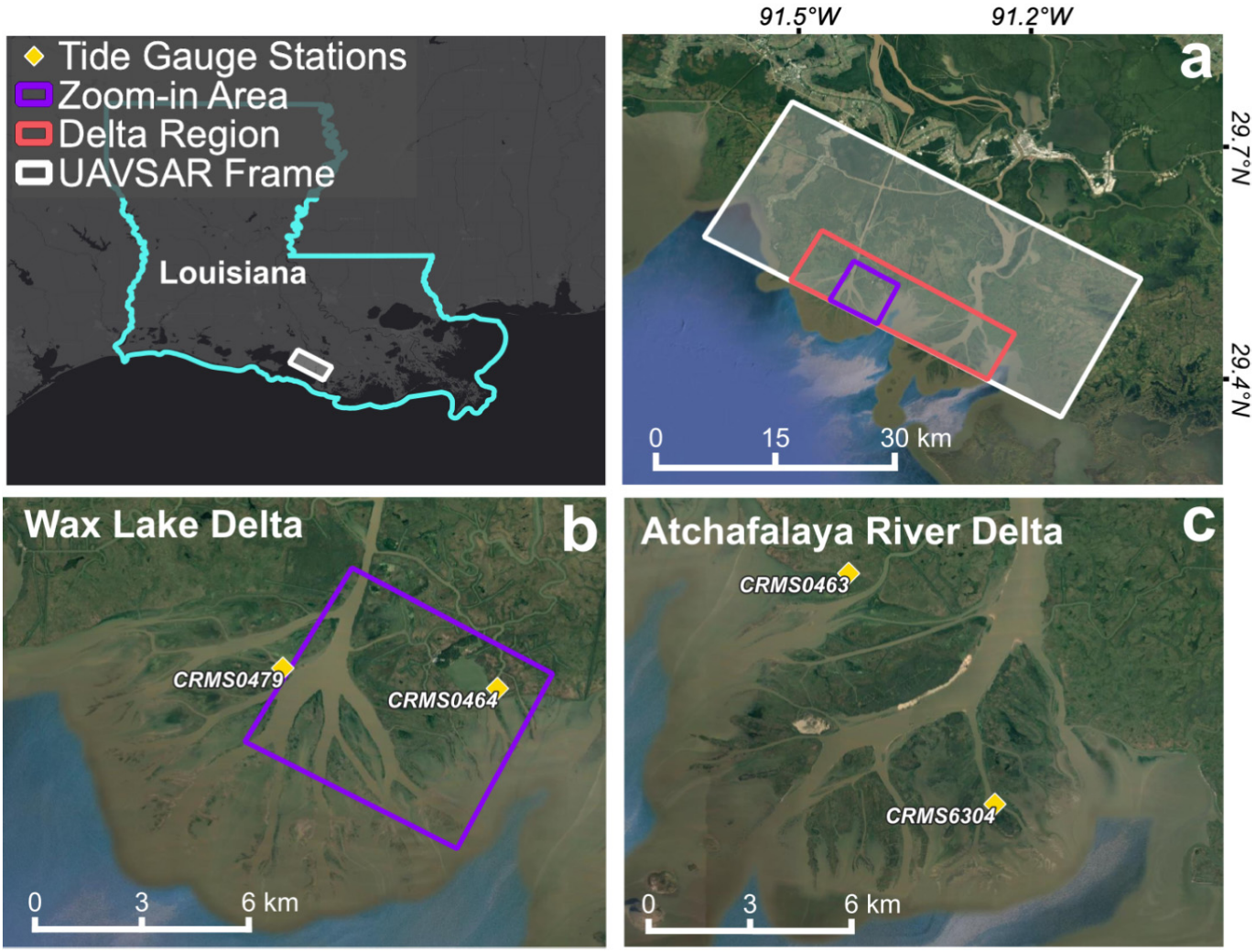

Fig. 1. Data location. The upper left map shows the regional overview. (a) and (b) White rectangle shows the full coverage of the UAVSAR imagery, the red frame shows the area analyzed for this study, which includes both the wax lake and Atchafalaya river deltas, and purple square shows the wax lake delta zoom-in area, centered toward the left edge of the wax lake delta. (b) and (c) Yellow rhomboids pinpoint the tide gauge stations used to compare InSAR results in the two deltas.

and NN + 2 interferograms with phases

$$\Delta\varphi^{w}_{\mathrm{NN}+2} \equiv \left\{\Delta\varphi^{w}_{i,i+3} \forall i \in (0, \ldots, m-3)\right\} \tag{7}$$

were formed. All interferograms are phase unwrapped using the 2-D, statistical-cost, network-flow algorithm for phase unwrapping (SNAPHU) [25] to obtain unwrapped phases for each. SNAPHU generates a mask of connected components. Each component is a collection of adjoined pixels considered reliably unwrapped in the spatial domain that is separated spatially from other connected components by decorrelated areas, e.g., open water channels around an island or areas with steep phase gradients that could not be unwrapped. Special considerations are taken to obtain the best possible results from the phase unwrapping algorithm. We provide to SNAPHU a coherence-based water mask calculated independently for each interferogram to aid the unwrapping process and improve the connected component mask definition. An interferometric coherence threshold was determined by analyzing the average spatial coherence of all generated interferograms, with values of coherence <0.4 considered to be open water, i.e., totally decorrelated [see Fig. 2(a)–(c)]. Because the data are highly coherent within wetlands and there are many channels and small islands, we increase the maximum allowable number of connected components and reduce the minimum connected component size in SNAPHU to better define the reliable groups of pixels within those small regions [26], [27] (extended examples on the impact of the steps abovementioned covering the full deltaic zone and an SNAPHU configuration file sample can be found in Supplementary Materials S1, S2, and S3). Connected components, while their unwrapped phase values are internally consistent, can have phases that differ by an arbitrary and unknown multiple of 2π, i.e., phase cycles, from other connected components. Although SNAPHU does not have an unwrapped phase error correction algorithm that adjusts the phases of the connected components relative to others, it is usually done manually or automatically, e.g., as implemented in the Miami InSAR Time-Series processing algorithm (MintPy) [13].

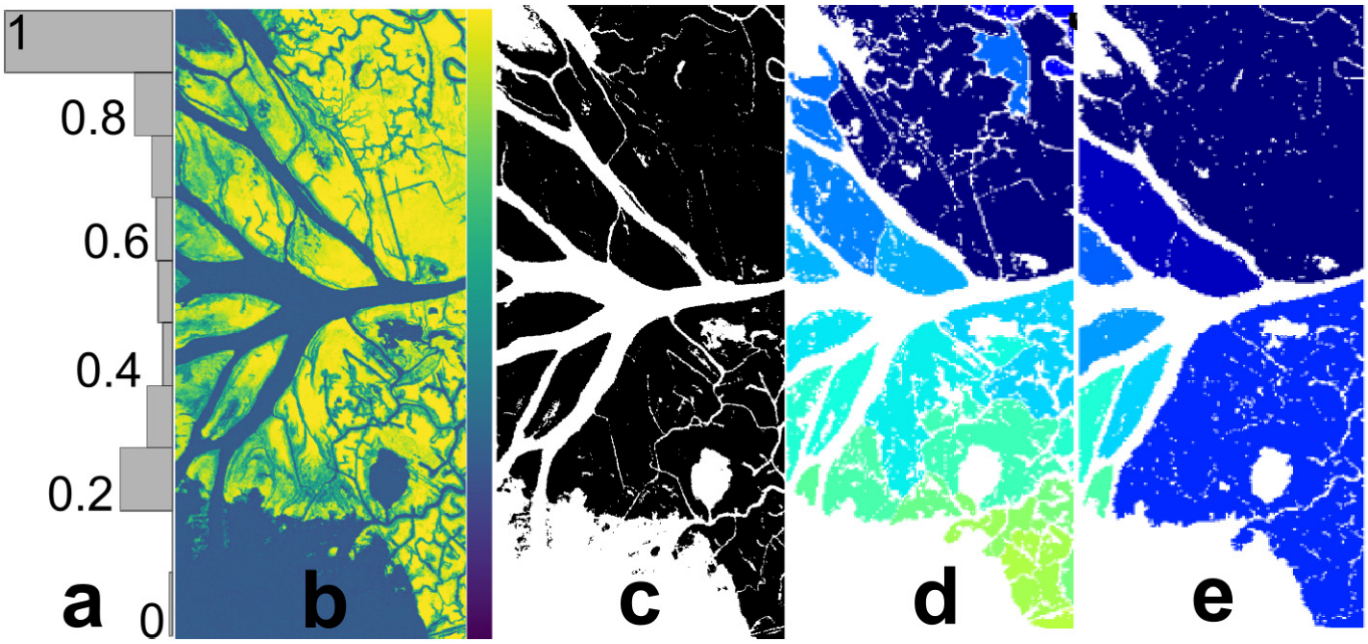

Fig. 2. Wax lake delta coherence-based water mask and connected components from SNAPHU. (a)–(c) Coherence histogram, coherence map, and coherence-derived water mask, respectively. (d) Resulting connected components from SNAPHU after implementing the coherence water mask and changing the default processing parameters to increase the number of connected components allowed and reduce their minimum size. (e) Example of the resulting connected components from SNAPHU if no adjustments are implemented.

Three interferogram stacks are generated to have increasing overlap and increasing temporal baselines. Each stack contains a network of interferograms. The NN network consists only of $\Delta\varphi^{w}_{\mathrm{NN}}$, the NN + 1 network consists of $\Delta\varphi^{w}_{\mathrm{NN}}$, $\Delta\varphi^{w}_{\mathrm{NN+1}}$, and the NN + 2 network consists of $\Delta\varphi^{w}_{\mathrm{NN}}$, $\Delta\varphi^{w}_{\mathrm{NN+1}}$, $\Delta\varphi^{w}_{\mathrm{NN+2}}$. The three networks are used to perform unwrapped phase error corrections iteratively within the algorithm presented in this work. In addition, using the three networks when estimating water-level change time series will aid in the reduction of atmospheric contributions, which are present in the region and vary at spatiotemporal scales that make correction infeasible. Given the temporal and spatial resolutions of the UAVSAR acquisitions used in this work, implementation of correction models [28]–[32] does not reach the spatial or temporal resolution of the observations. Our correction algorithm consists of an iterative process using bridging between islands (spatial domain) and phase closure between interferograms (time domain). The bridging algorithm uses the spatial relationship of phase within a group of pixels to correct unwrapping errors. Phase closure uses the phase relationship in time between temporally overlapping interferograms for a single pixel to find the correct phase cycle. Both steps are discussed in detail in later sections. The correction steps are implemented prior to the InSAR time-series retrieval and after the SNAPHU phase unwrapping, as shown in the workflow schematic (see Fig. 3). Water level change time-series estimations are retrieved using the small baseline subset (SBAS) algorithm [33] as implemented within MintPy [13]. We evaluate the performance of our unwrapping algorithm by generating a temporal coherence map [34]. Temporal coherence analysis provides a quantitative assessment of the pixels that were correctly unwrapped versus those that still have unwrapping errors and, thus, can be used in quality assessment of the derived water level change time series. Finally, a comparison of InSAR-derived water level change and CRMS tide gauge water level change is performed as ground validation.

The unwrapping correction process starts with the NN network, which is expected to have the least number of unwrapping errors of the three sets, since it involves the smallest amount of water level change and the least temporal decorrelation. First, a minimum spanning tree (MST)-based bridging correction is applied to the NN interferometric network to remove possible phase discontinuities present in the space domain. MST bridging forms part of the standard MintPy algorithm [13]. NN interferograms are considered a reliable base to start the correction process, and for our dataset, coherence is well maintained and phase gradients low even along the coast. No phase closure is applied at this step because no temporally overlapping acquisitions were included in this network. Next, the algorithm is applied to the NN + 1 network, which now includes the corrected NN interferograms, and the next iteration is applied to the NN + 2 networks, which now included corrected NN and NN + 1 interferograms. With temporally overlapping interferograms, we benefit from the relationship in time between triplets of interferograms to localize and isolate the regions of unwrapping error. At this point, phase closure of interferogram triplets is estimated. The phase closure of interferogram triplets, C^{u}, is defined as the cyclic product of unwrapped interferograms. For example, for $\varphi_{(0:2)}$, it can be expressed as

$$C^{u} = \Delta\varphi^{u}_{01} - \Delta\varphi^{u}_{02} + \Delta\varphi^{u}_{12}. \tag{8}$$

From this relationship, it is possible to estimate the phase closure integer ambiguity by comparing the wrapped triplet

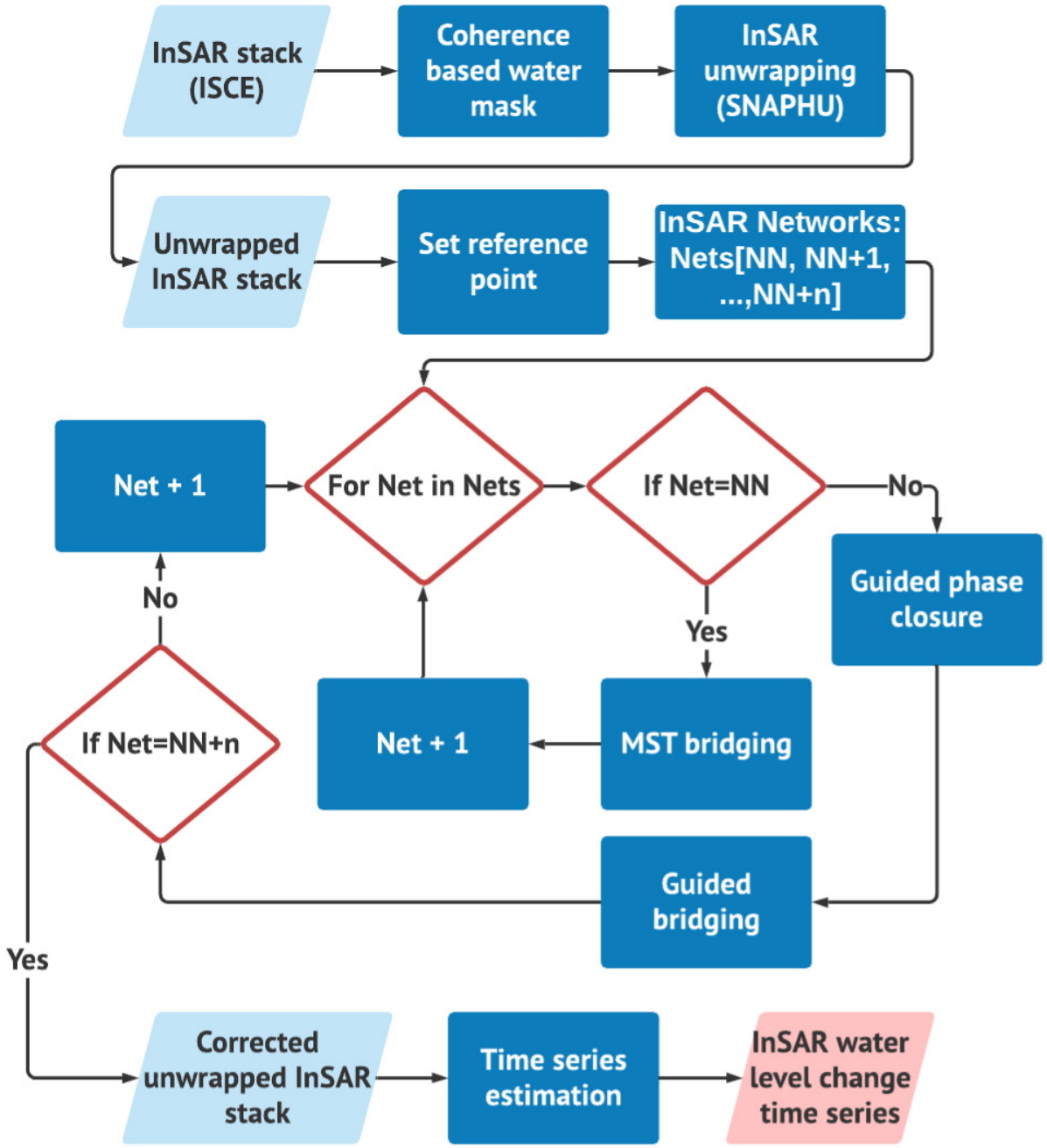

Fig. 3. InSAR water level change time-series processing workflow. The steps in light blue represent inputs, while the dark blue squares are processes. The red parallelogram is the final output.

closure phase against the unwrapped one as follows:

$$C_a = \frac{C^u - C^w}{2\pi} \tag{9}$$

where C^w is the wrapped $[-\pi$ to $\pi)$ triplet closure phase and C_a is the triplet closure phase integer ambiguity, which is equal to zero if no unwrapping error is present. A C_a map is generated for each triplet and used as a guide throughout both bridging and phase closure correction algorithms. Regions that show $|C_a| \geq 1.0$ values are defined as error regions and separated for correction.

A. Guided Bridging

When unwrapping errors occur in areas where contiguous pixels are unwrapping error-free, one can take advantage of the spatial relationship between pixels and use the error-free regions to estimate the phase offset required to correct the incorrectly unwrapped areas [13], [27]. For the case of our study area, we assume that the different observed islands are not hydrologically independent, so similar changes in water level are expected across the entire landscape. This assumption is particularly true for the L-band,

having a 23.8-cm wavelength, and for acquisitions with 30-min separation. In our algorithm, we exploit the pixel spatial relationship by connecting groups of pixels defined by the connected components formed as part of the unwrapping process [25]. The C_a mask is used to define the regions that require corrections. Three bridges are formed connecting the component containing unwrapping errors with the nearest error-free connected components. A standard deviation mask based on the statistics of the spatial coherence calculated from the NN + 1 or NN + 2 sets of interferograms, depending upon the set currently being added to the network (see Fig. 3), is used to select the bridged error-free component with minimum standard deviation for each iteration. The selected component is used to estimate the integer-cycle phase offset between the two ends of the bridge. To avoid very steep phase gradients found toward the edges of wetland islands, we implemented an image edge-erosion algorithm proposed by Yunjun *et al.* [13]. This ensures that the two ends of the bridge do not fall in an area with a high phase gradient. Fixed windows centered at the two ends of the bridge are used to estimate the median phase value, which is then used to calculate the integer 2π phase difference between the bridged correct region and the region with the error. To facilitate language throughout this article, we will use bridging to refer to guided bridging. An example is shown in Fig. 4.

B. Guided Phase Closure

The phase closure error correction algorithm is performed by taking samples from the areas that require corrections, exploiting the relationship of interferometric phase in time. These areas are defined by the C_a mask. A set of random samples proportional to the size of the region to be corrected is used to estimate the integer-cycle phase offset. The median value of the interferogram triplet is used to estimate the phase jump. The estimated correction for each region is then applied only to the newly added interferograms in this iteration (NN + 1 phases for the NN + 1 network and NN + 2 phases for the NN + 2 network). To facilitate language throughout this article, we will use phase closure to refer to guided phase closure. An example is shown in Fig. 4.

C. Iterative Phase Correction

Both the bridging and phase closure algorithms can be applied independently or successively together as a complement to each other (see Fig. 4). Corrections are only applied to the new interferograms added in each network increment. In each iteration, the previous set of interferograms is assumed to be correct, starting from the bridge-corrected NN interferograms, correcting for NN + 1 and repeating until NN + n interferograms have been corrected. The MintPy SBAS time-series algorithm is then applied to the set of corrected unwrapped phases to estimate the water level change at each epoch (time of acquisition), starting from zero water level at the time of the first acquisition. A temporal coherence map is generated as a quality assessment within the time-series estimation process. Temporal coherence, γ, is generated by constructing interferograms using the time-series estimation results for the epochs to compare against the original interferograms and is defined as [34]

$$\gamma = \frac{\left|\sum_{p=0}^{M-1} e^{\imath\left(\Delta_\varphi - \Delta_\varphi^\gamma\right)}\right|}{M} \tag{10}$$

where $\Delta\varphi^r$ is the interferometric phase reconstructed from the estimated water level change time series and M is the number of interferograms. Values of γ close to 1 are unwrapped correctly, while γ values near zero correspond to poorly unwrapped pixels. The temporal coherence map allows us to evaluate the performance of the unwrapping correction algorithm, and in addition, it can be used as a mask to remove the remaining unreliable pixels from the final water level change time-series estimation.

D. Tide Gauge Validation

Cross validation of the time-series results was performed by comparing InSAR-derived water level change and water levels measured at tide gauge stations within the study area. We use a fixed pixel window (4 × 4) centered at the latitude and longitude of the corresponding CRMS tide gauge to estimate a mean InSAR-derived water level change. Special considerations were taken for station CRMS0479, where a window of 50 × 50 pixels was used due to the tide gauge location (in the middle of a large channel, in open water). A linear interpolation of the CRMS stations' measurements (hourly) was performed to match the acquisition time from UAVSAR (∼30-min rate) and obtain the corresponding water level. Finally, we adjust the InSAR time series to match the water level measured by the tide gauge (w_g) at the time of the first acquisition [$w_g(t0)$]

$$w(t) = \Delta w(t) + w_g(t0). \tag{11}$$

IV. Results

A set of six SAR acquisitions was processed to test the presented unwrapping algorithm. Corrections were applied to NN, NN + 1, and NN + 2 networks of interferograms using one or both phase closure and bridging (e.g., Figs. 5 and 6) to evaluate the performance of each correction. Water level change time series was derived from the NN + 2 networks corrected results (see Fig. 7).

Bridging correction results alone were found to be insufficient to fully correct the interferogram [see Fig. 4(e)–(g)]. This is mainly due to the specific characteristics of the study area, being a river delta with a high rate of water level change during a tidal cycle and with many disconnected islands. Nevertheless, for the example shown in Fig. 4, it was able to compensate for many of the errors located toward the edge of the Wax Lake Delta, observed as the differences between C_a maps (d) and (g). Phase closure alone had better performance, correcting for most of the errors found in both deltas [see Fig. 4(h)–(j)]. Nonetheless, some small areas are left uncorrected with either bridging or phase closure alone and can be corrected by combining phase closure and bridging [see Fig. 4(k) and (l)]. An overview of the full workflow of corrections (see Fig. 5) and performance comparisons (see Fig. 6) for each iterative step for the full set of NN, NN + 1,

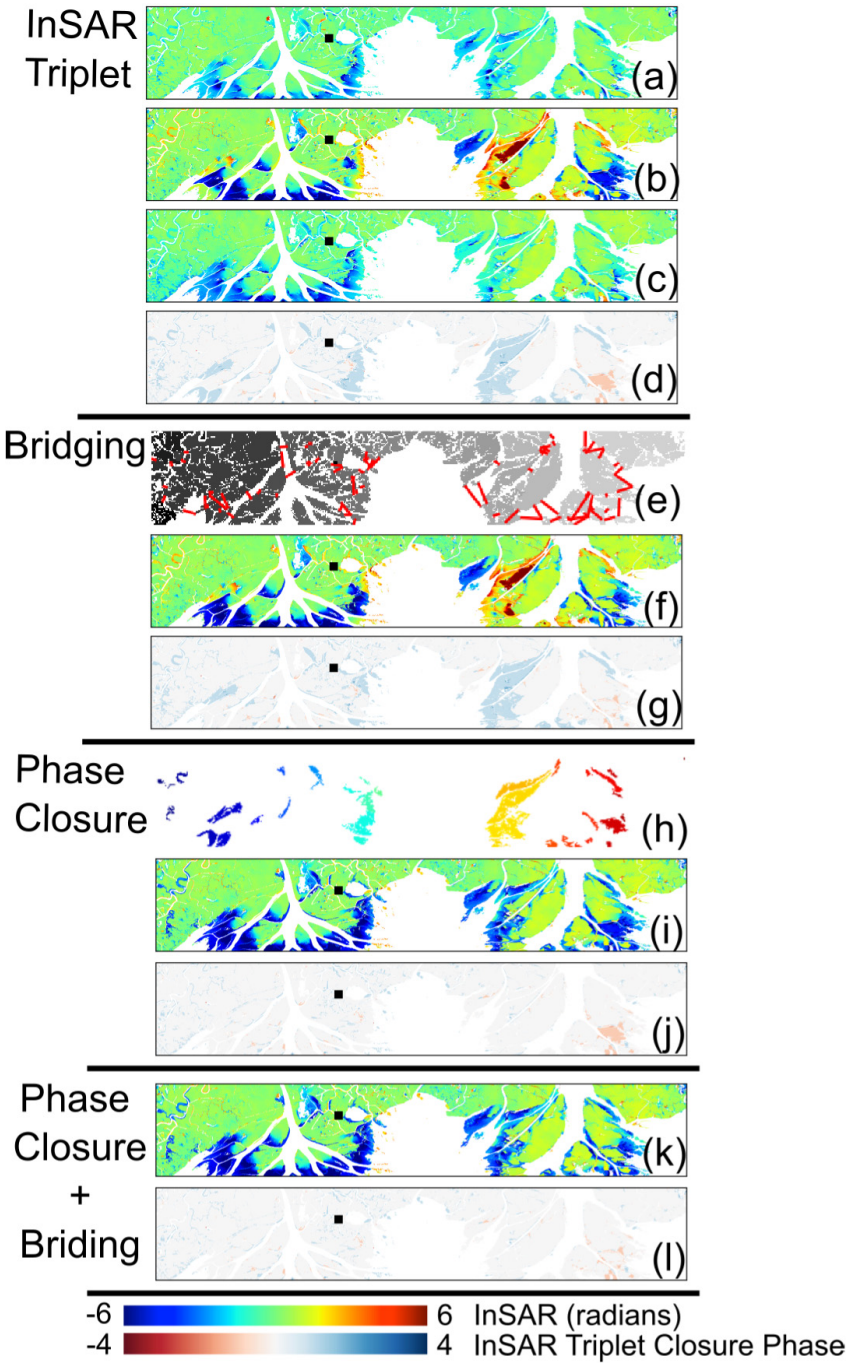

Fig. 4. Unwrapped interferogram triplet and phase correction example. (a)–(c) Unwrapped interferograms that form a triplet. In this example, (a) is the NN interferogram with phase change $\Delta\varphi_{23}$, (b) is the interferogram to be corrected, in this case, NN + 1 interferogram with phase change $\Delta\varphi_{24}$, and (c) is the NN interferogram with phase change $\Delta\varphi_{34}$. The C_a map from the triplet is shown in (d). The bridging correction (alone) for (b) interferogram is shown in (e)–(g), where (e) shows the bridges on the connected component map for the areas with phase unwrapping errors, (f) shows the bridging-corrected interferogram, and (g) shows the C_a map after the bridging correction is applied. The phase closure correction (alone) is presented in (h)–(j) images. (h) Extracted regions from (d) C_a, which were sampled to perform the phase closure correction. (i) Interferogram shows the result of the phase closure correction algorithm. (j) C_a map after correction. (k) and (l) Result of applying phase closure first and bridging afterward (together): (k) shows the resulting corrected interferogram and (l) shows the C_a map after corrections.

and NN + 2 interferograms encompassing all five acquisitions is presented. Fig. 6 shows the corrections using bridging alone, phase closure alone, or both (similar examples for the Atchafalaya River Delta can be found in Supplementary Materials S4 and S5).

Results shown in Fig. 5 highlight the improvements achieved by implementing the full sequence of the iterative unwrapping correction algorithm on NN, NN + 1, and NN + 2 interferograms. It also helps to identify the regions that are most likely to have unwrapping errors, such as

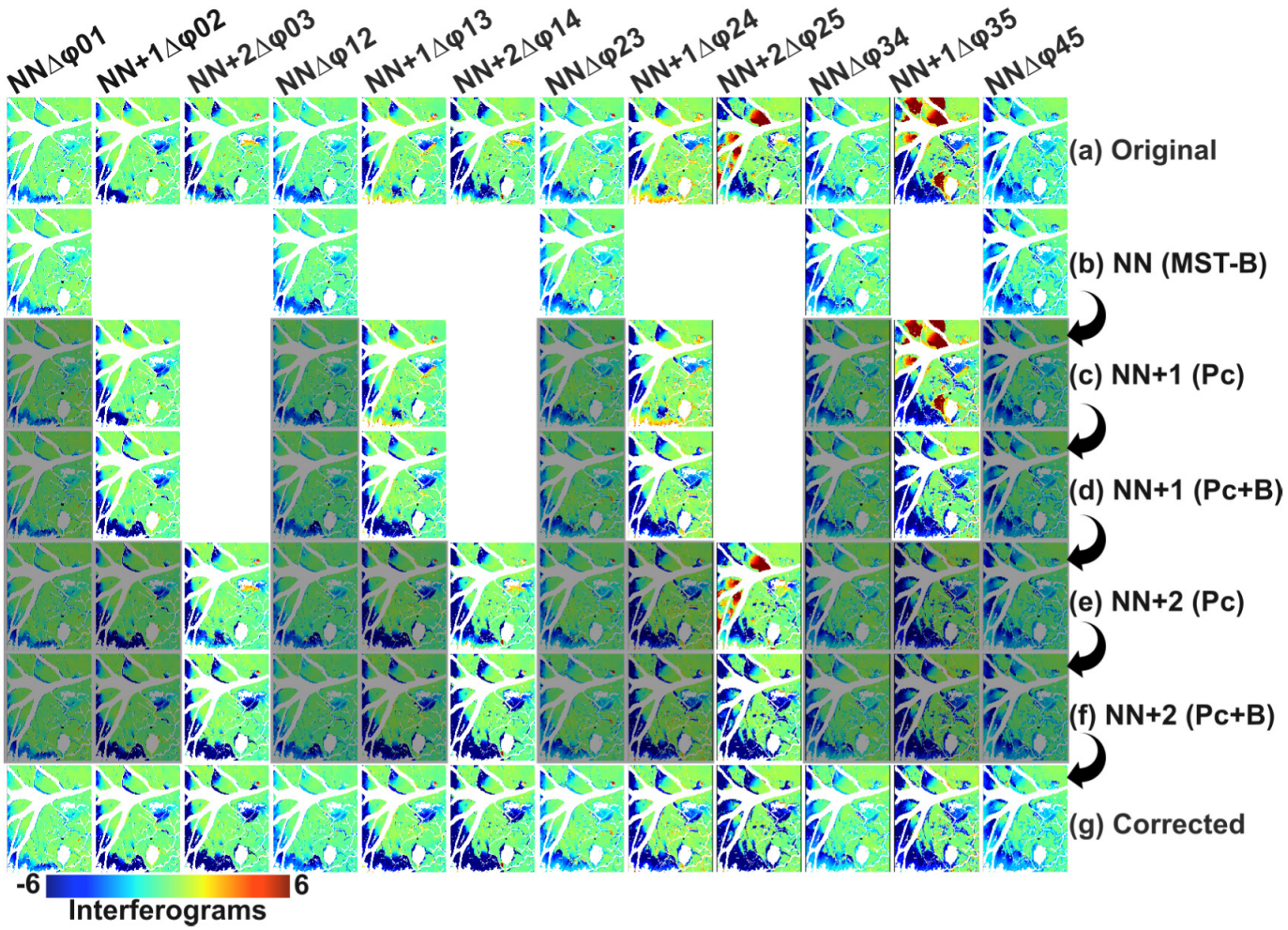

Fig. 5. Full sequence of phase corrections for the network of NN, NN + 1, and NN + 2 unwrapped interferograms for the case pf six acquisitions. (a) All NN + 2 interferograms without corrections (original). (b) Shortest temporal-baseline interferograms NN to which MST bridging is applied [NN (MST-B)]. (c) and (d) Add the uncorrected NN + 1 interferograms and show (c) phase closure (Pc) [NN + 1 (Pc)] and (d) phase closure + bridging (Pc + B) correction steps [NN + 1 (Pc + B)], respectively. (e) and (f) Add the uncorrected NN + 2 interferograms and show (e) phase closure (Pc) [NN + 2 (Pc)] and (f) both phase closure and bridging (Pc + B) corrections[NN + 2 (Pc + B)]. Shaded interferograms in rows (c)–(f) represent interferograms that were already corrected in previous steps. (g) Fully corrected interferograms.

the edges and center of deltaic islands in the Wax Lake Delta (see Fig. 5). A detailed view of the improvements obtained in each correction step is shown in Fig. 5, where C_a maps of each triplet and temporal coherence plots are presented.

Improvements from each correction can be hard to track visually at the scale shown because, in many cases, the corrected features are small and dispersed across the interferogram. However, it is possible to see the improvements in temporal coherence, shown at the right hand end of each row (see Fig. 6). The performance correction overview highlights that, even though the bridging correction does a good job, large errors remain in the Wax Lake delta. Conversely, phase closure applied alone shows better results. However, the best performance is obtained by the combination of both phase closure and bridging, visible when looking at the temporal coherence of bridging, phase closure, and phase closure + bridging from examples in network NN + 2 [see Fig. 6(f)–(h)]. InSAR-derived results show relative water levels of higher than 20 cm (see Fig. 7). The largest rates of change can be observed toward the edges of the deltaic islands (red/orange colors), which happens to be the region with the most phase unwrapping errors, as shown in previous figures. This is because the vegetation type and location of these areas allow for more exposed tidal interactions than inner wetlands, in which few unwrapping errors were observed.

Scatterplots comparing measurements between tide-gauge and calibrated InSAR-derived water level show a root mean square error (RMSE) lower than 3 cm for all stations except CRMS0479, which has an RMSE of 4.14 cm. Tide gauge CRMS0479 is located in an area where the two adjacent islands have high phase gradients. Moreover, the tide gauge is located in the channel between the islands in an area without emergent vegetation, making it difficult to properly capture the same water level change measured by InSAR. The tide gauges at all CRMS stations in the study area were in a channel at the edge of the wetlands, which complicates a one-to-one comparison between InSAR-retrieved water level change and

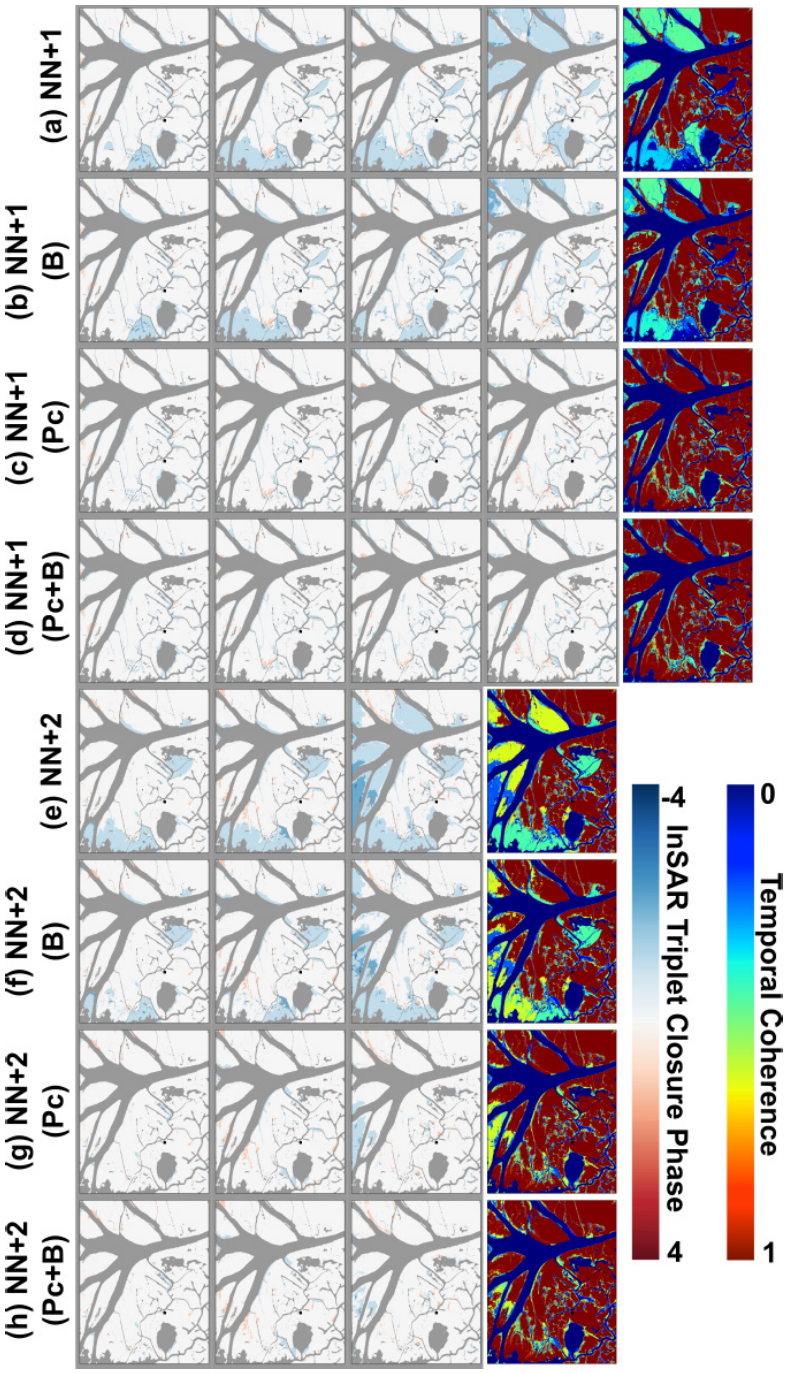

Fig. 6. Correction performance overview. C_a maps of each triplet and temporal coherence (Tc) maps (last square to the right of each row) used in each correction. (a)–(d) NN + 1 C_a and Tc maps, where (a) is the uncorrected network (NN + 1), (b) after bridging (B) [NN + 1 (b)], (c) after phase closure (Pc) [NN + 1 (Pc)], and (d) after phase closure and bridging (Pc + B) corrections [NN + 1 (Pc + B)], respectively. (e)–(h) NN + 2 C_a and Tc maps, where (e) is the uncorrected network (NN + 2), (f) after bridging (B) [NN + 2 (B)], (g) after phase closure (Pc) [NN + 2 (Pc)], and (h) after phase closure and bridging (Pc + B) corrections [NN + 2 (Pc + B)], respectively. Blue and red in the C_a maps show negative and positive integers' phase offsets from each triplet, respectively. Red in the Tc maps show correctly unwrapped regions, while yellow green and light blue areas show poorly unwrapped regions. Values near zero (dark blue) show totally uncorrelated areas, in this case water.

the tide gauges used for validation. This topic is discussed in Section V.

V. Discussion

We find that the proposed unwrapping error algorithm corrects most of the unwrapping errors in the interferograms, as shown in Fig. 6. InSAR-derived time-series results and tide gauge measurements show good agreement, with RMSE values of under 3 cm for three of four stations. However, as mentioned previously, the tide gauges are installed in channels, complicating the comparison. Station CRMS0479 is used as an example to illustrate this issue and to contrast the conditions at that station to those at the other three. The CRMS0479 gauge is located between two wetland islands

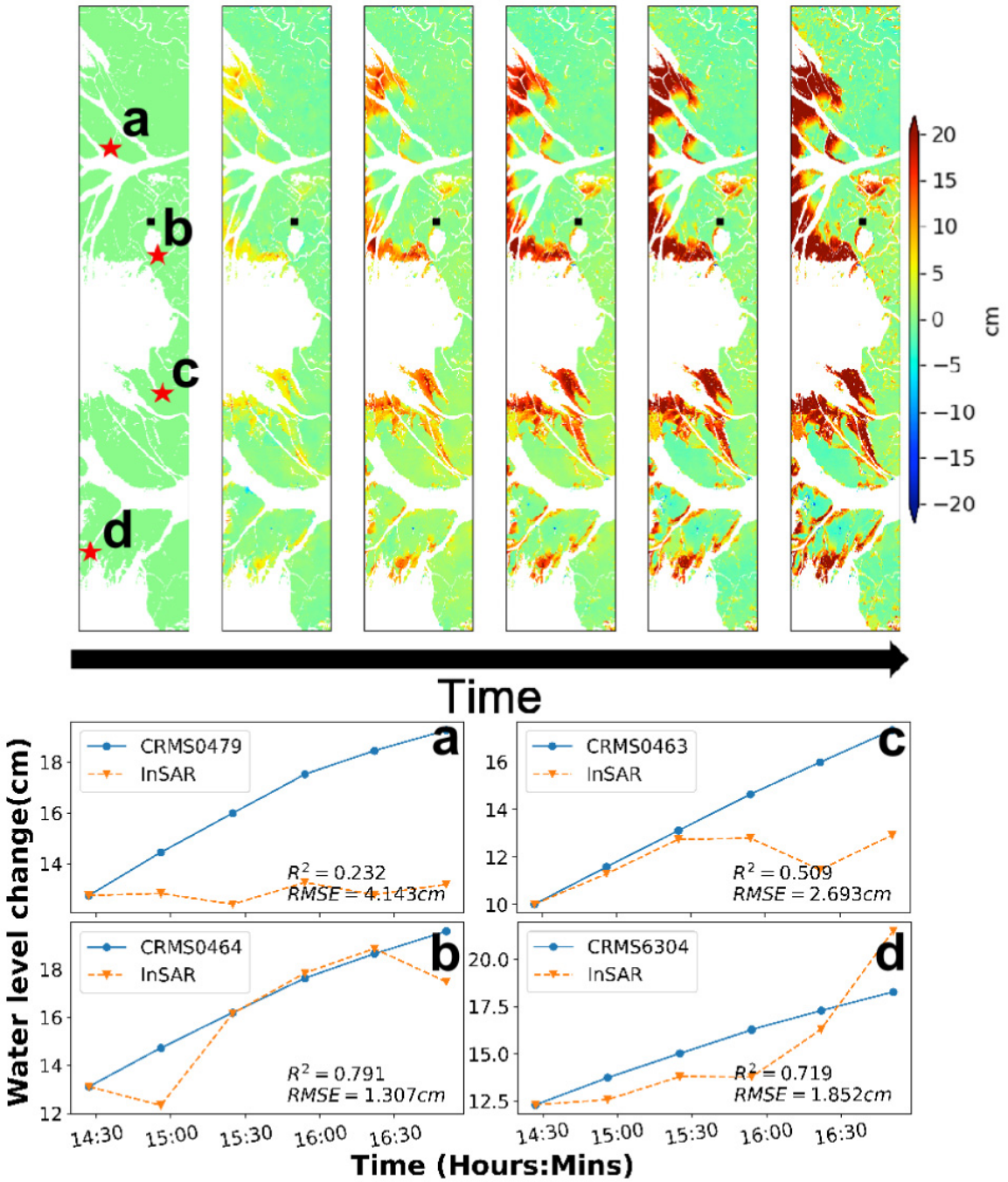

Fig. 7. InSAR-derived water level time-series (upper row). Red stars a, b, c, and d correspond to the location of the CRMS tide gauges available for the region. Below that are plotted the InSAR-derived mean $w_{(t)}$ water level change as a function of time (orange line) calculated by averaging over a 4 × 4 pixel window centered at the tide gauge locations a, b, c, and d. The CRMS stations water levels (blue line) are shown in each plot. R^2 and *RMSE* estimations for each InSAR-derived mean $w_{(t)}$ and CRMS water level are provided at the bottom right corner of each plot.

near the edge of the Wax Lake Delta (see Fig. 8). From the reference location map in Fig. 8(b), the station appears to be closer to the edge of the South Island. A detailed look into the tide gauge information available on the CRMS website revealed that the station is located roughly 8 m away from the south island's edge and approximately 88 m from the north island [see Fig. 8(d)]. The InSAR-derived water level change shows a marked difference between the two islands. Mean $w_{(t)}$ estimated using a 4 × 4 pixel window centered at the tide gauge and two more at the same latitude but within the north and south islands show a difference in water level change between islands larger than 30 cm (see Fig. 8).

At CRMS0479, the observed water level change patterns between both islands may correspond to a combination of factors, such as differences in vegetation type, elevation, and the presence of natural or man-made structures (e.g., levees). As a result, water flow patterns through wetlands will vary from what is registered by the gauges in the open water. While CRMS0479 recorded a water level of ∼20 cm in the last timestamp, the samples taken at the south and north islands

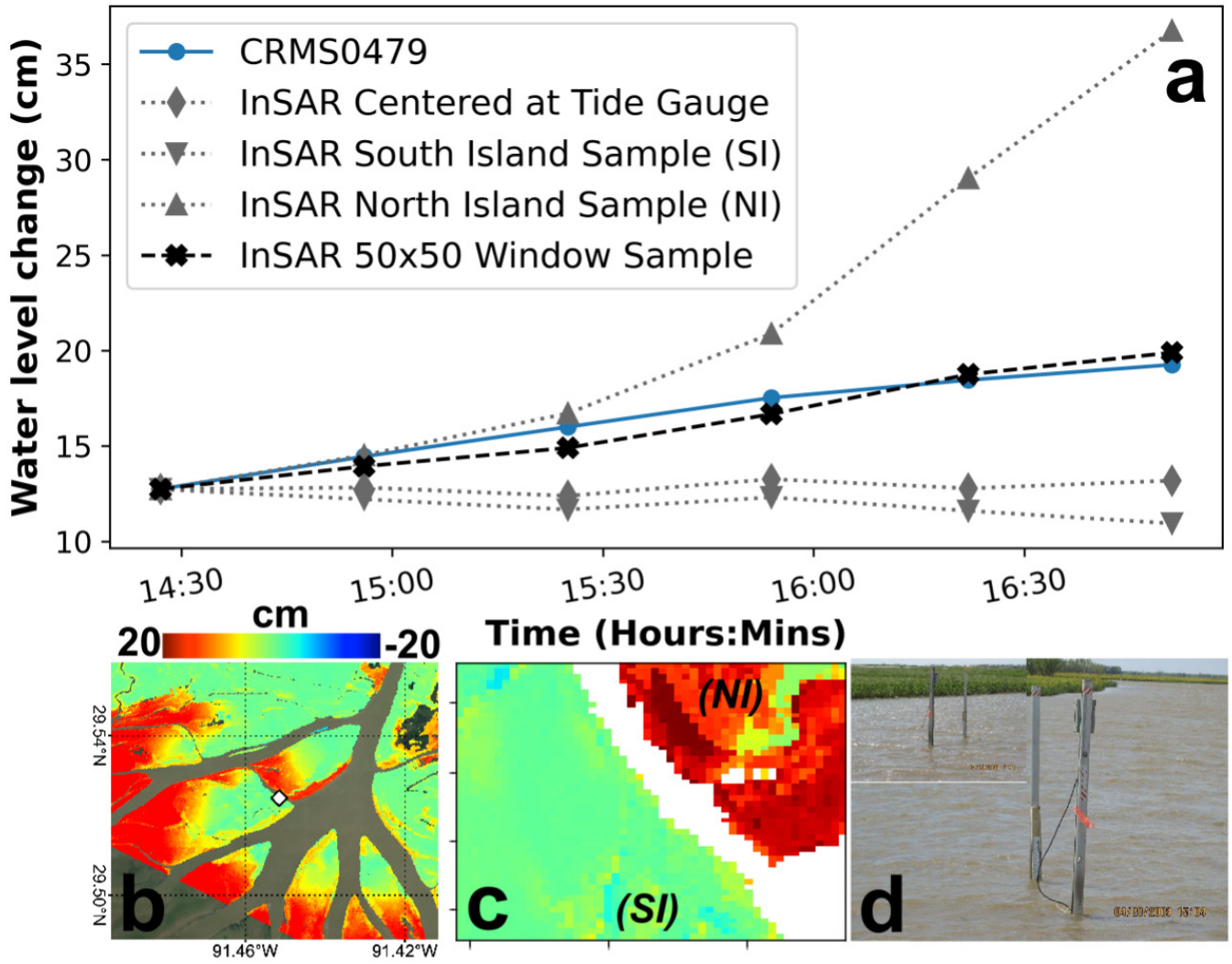

Fig. 8. InSAR-derived water level time-series comparison at CRMS0479 location. (a) Mean $w(t)$ water level change using a 4 × 4 pixel window sample from the center of the tide gauge and nearby on the north and south islands (gray lines). A regional sample of mean $w(t)$ water level change centered on the gauge and encompassing both islands was estimated using a 50 × 50 pixel window (black line). Corresponding CRMS0479 station water level is shown with a blue line. InSAR maps (b) and (c) provide an overview of InSAR-detected water levels within the wax lake delta and in both the north and south islands near CRMS0479 (white diamond). Map (c) shows the pixels used to estimate mean $w(t)$ using a 50 × 50 window. In this window, water pixels are masked out and not considered in the estimation. Photograph (d) of tide gauge CRMS0479 was taken from the reports at https://www.lacoast.gov/CRMS.

reflect ∼10 and ∼35 cm, respectively (see Fig. 8), highlighting the importance of locating tide gauges within the wetlands to improve ground-truthing. To illustrate the ambiguity, we utilized a larger sampling window (50 × 50 pixels centered at the station location) that included segments of both islands near the station [see Fig. 8(a)]. Results of this comparison yielded a very close approximation to what the tide gauge registered, with an RMSE of 0.67 cm, the lowest at all stations. Given the low RMSE obtained from the 50 × 50 samples and the fact that both north and south islands were corrected through the implementation of the enhanced algorithm (as shown by the temporal coherence in Fig. 6), we use this sample for the examples further on.

In addition to testing the algorithm on challenging areas, we tested its performance in areas where SNAPHU performed well. A water level time-series comparison was performed between uncorrected interferograms, interferograms corrected implementing [13], and those corrected using the new algorithm over two regions near tide gauge locations: one that required phase unwrapping corrections [see Fig. 9(c) and (f)] and one that did not [CRMS4808; see Fig. 9(b) and (d)]. Station CRMS4808 is located north of the Wax Lake Delta, further inland from the coast, and did not present visible unwrapping errors. Station CRMS0479, located between two islands at the Wax Lake Delta, did require corrections. Both algorithms, [13] and the one presented in this article, make use of the bridging and phase closure approach. However, the approach of Yunjun *et al.* [13] corrects all interferograms at once, unlike our proposed sequence, namely, iterations with an increasing number of connections in the network. Yunjun *et al.* [13] use all available interferograms and an L1-norm regularized least-squares optimization to implement phase closure. It also implements a single-bridge per component approach based on a minimum spanning tree (MST)

weighted graph that associates connected components by size from larger to small using the shortest possible distance bridge. Results from the comparison show the improvement achieved by each algorithm throughout the correction steps presented in this article (see Fig. 9).

Observations from the inland station CRMS4808 show the same phase as a function of time through all corrections and methods [see Fig. 9(b)], showing little to no phase unwrapping errors present in this region. Conversely, station CRMS0479 is right at the river delta [see Fig. 9(f)], where higher phase gradients and low coherence-driven disconnections are expected. Phase unwrapping in this region required correction, and as shown in Fig. 9(e), considerable differences can be observed among the correction algorithms. Results from [13] show small changes after applying only phase closure (RMSE of 2.98 cm) and noticeable overcorrection when applying bridging and phase closure (RMSE of 4.72 cm) (shown as "B + PC"). Results from the presented algorithm show small improvements after correcting the NN + 1 interferograms (RMSE of 1.41 cm), which improves after the next iteration for NN + 2, with almost no difference between phase closure and phase closure + bridging corrections (shown as "PC + B") (RMSE of 0.67 cm in both cases). This comparison not only helps to illustrate the differences between correction algorithms but also highlights the performance of the phase closure corrections implemented. Both C_a mask and temporal coherence are very useful resources for mapping unwrapping errors. However, because they are both intrinsically linked to the temporal relationship of the interferograms, they are not as effective in assessing the quality of the phase closure algorithm as it also exploits the InSAR temporal relationship. Thus, it is important to also compare the InSAR observations against *in situ* data, such as tide gauges, to further assess the correctness of the InSAR-derived measurements.

Performance comparison between corrections (see Table I) reveals that, for the deltaic region (red rectangle in Fig. 1), 51% of the pixels have temporal coherence equal to or higher than 0.7 from the uncorrected NN + 1 network. For comparison, after performing all corrections, 86% of the pixels display a temporal coherence value equal or higher than 0.7 for the NN + 1 network and 81% for the NN + 2 network (see Table I).

Comparisons shown in Table I(b) highlight the improvements achieved by the proposed algorithm in comparison with the ones of [13] for which 65.3% of pixels (3.103 cm RMSE) had temporal coherence above 0.7 after all corrections. That is 16% lower than the results obtained by our iterative approach (1.791-cm RMSE). Even though some interferograms may only require the implementation of the bridging algorithm or phase closure alone, the use of both corrections together gave the best results for the water level change retrieval presented in this work. Applying phase closure correction first and bridging second yielded better correction performance with the new algorithm, whereas the opposite is true for the algorithm in [13], which has significantly poorer performance [see Table I(b)]. For our algorithm, implementing bridging alone showed an improvement of 10% in temporal coherence (2.614-cm RMSE), whereas applying only phase closure returned an improvement of 34% more pixels (1.785-cm RMSE) than bridging. If we compare performance between applying bridging or phase closure first, we observe that, for implementing bridging first and phase closure second, 85% of the pixels are higher or equal than 0.7 temporal coherence (3.077-cm RMSE). In contrast, if phase closure is applied first and bridging second, 86% of pixels are reliably corrected (1.785-cm RMSE). This difference is because the phase closure algorithm does a good job correcting most major unwrapping errors, and bridging then can correct the small isolated islands remaining. Conversely, if bridging is applied first, a mixture of small and large areas may be left without being corrected due to the large volume of unwrapping errors, and then, the phase closure algorithm may not be able to correct all small isolated features. Corrections for NN + 2 interferograms showed an improvement in temporal coherence of 29% between interferograms without correction and phase closure and bridging corrections. Phase closure correction alone showed a good performance correcting for 28% of pixels. Estimated RMSE, in this case, shows no difference due to the sparse location of the tide gauge stations, not able to cover the full extent of the deltas like InSAR does. The observed difference between the new iterative algorithm and the algorithm of [13], currently implemented in MintPy, arises from fundamental differences between how each of them approaches phase unwrapping corrections. The bridging algorithm in [13] creates single-bridge MST connections between all connected components from large to small. A similar

TABLE I

PERFORMANCE COMPARISON TABLE DIVIDED BY (a) GUIDED ITERATIONS AND (b) COMPARISONS. GUIDED ITERATIONS' SECTION SHOWS THE PERFORMANCE OBTAINED THROUGHOUT THE CORRECTION STEPS OF THE GUIDED ALGORITHM PRESENTED IN THIS ARTICLE. COMPARISONS SECTION SHOWS THE PERFORMANCE OBTAINED FROM DIFFERENT COMBINATION OF CORRECTION STEPS PERFORMED USING BOTH THE GUIDED PHASE UNWRAPPING ALGORITHM AND [13]. PERFORMANCE IS MEASURED IN PIXEL NUMBER OR PERCENTAGE ABOVE 0.7 AND ALSO IN RMSE FROM COMPARING THE INSAR-DERIVED MEASUREMENTS AGAINST CRMS TIDE GAUGE STATIONS WITHIN THE WAX LAKE AND ATCHAFALAYA DELTAS (RED RECTANGLE IN FIG. 1)

(a)

Dataset	TC(pixels)>0.7	TC(pixel%)>0.7	InSAR vs Gauge RMSE
NN+1	1020967	51.09%	3.077cm
NN+1(Pc)	1706035	85.36%	1.785cm
NN+1(Pc+B)	1723944	86.26%	1.785cm
NN+2	1068165	53.45%	2.062cm
NN+2(Pc)	1609538	80.54%	1.791cm
NN+2(Pc+B)	1628612	81.49%	1.791cm

(b)

Dataset	TC(pixels)>0.7	TC(pixel%)>0.7	InSAR vs Gauge RMSE
NN+1(Guided B)	1220890	61.09%	2.614cm
NN+1(Guided Pc)	1706035	85.36%	1.785cm
NN+1([12] MST)	903512	45.21%	2.381cm
NN+1([12] Pc)	1162010	58.14%	3.077cm
NN+1(Guided B+Pc)	1697645	84.94%	3.077cm
NN+1(Guided Pc+B)	1723944	86.26%	1.785cm
NN+1([12] B+Pc)	1014943	50.78%	3.103cm
NN+1([12] Pc+B)	903512	45.21%	2.381cm
NN+2(Guided Pc)	1609538	80.54%	1.791cm
NN+2(Guided Pc+B)	1628612	81.49%	1.791cm
NN+2([12] Pc)	1199873	60.04%	3.225cm
NN+2([12] B+Pc)	1305073	65.3%	3.103cm
NN+2([12] Pc+B)	825603	41.31%	2.48cm

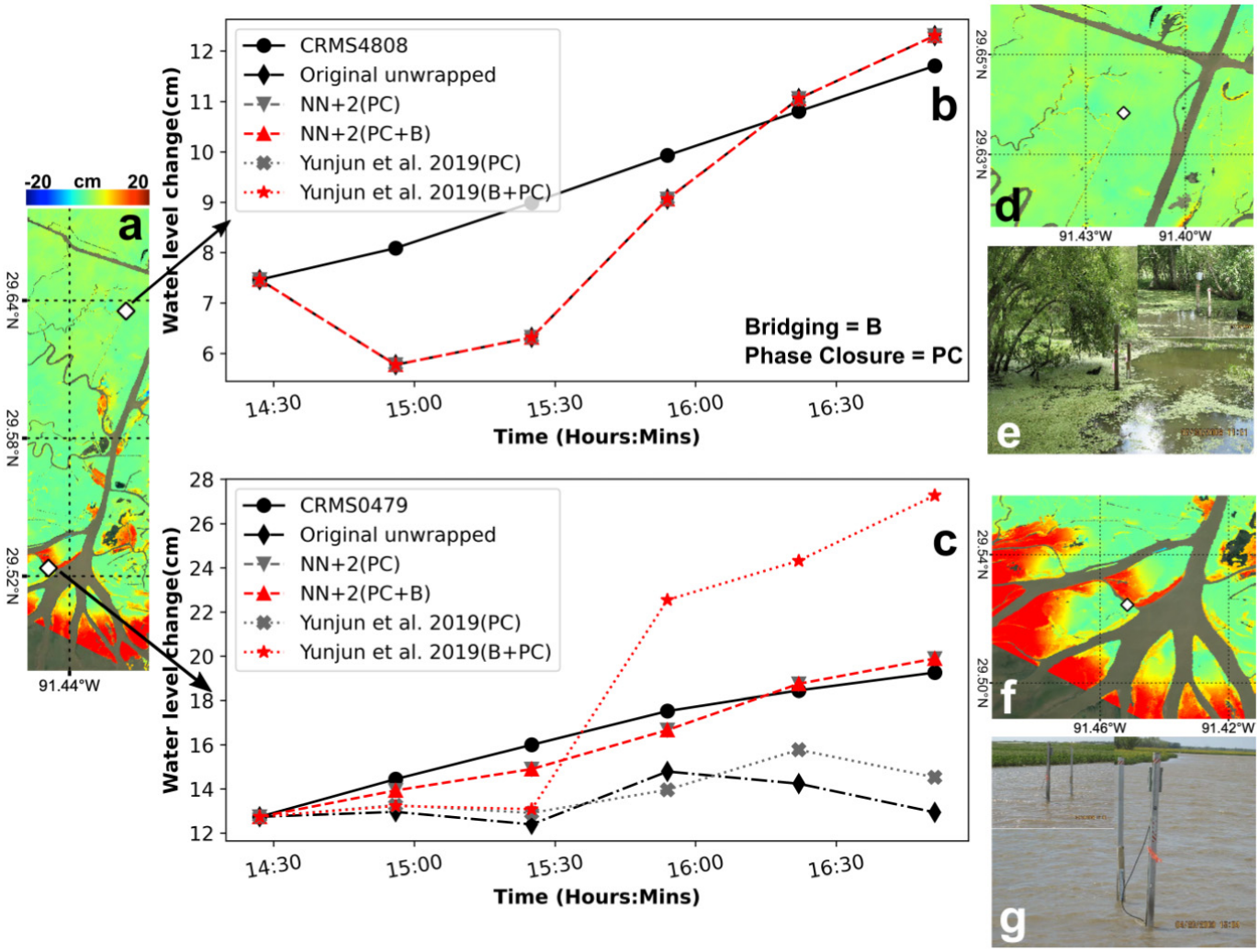

Fig. 9. (a) InSAR and CRMS reference location map. (b) and (c) Water level change comparison between InSAR-derived results and CRMS4808 and CRMS0479 tide gauges, respectively. Time-series with "◇" marker was generated using the original interferograms without corrections. Time series with gray crosses and red stars show the result of applying phase closure and bridging + phase closure corrections using the [13] algorithm. Gray downward-pointing triangles show results with phase closure correction applied to NN + 2. The red upward-pointing triangles are the final estimations from the fully corrected set of interferograms (phase closure and bridging). (d) and (f) Location of the CRMS4808 and CRMS0479 stations overlain on the InSAR water level at the final time step. (e) and (g) Photographs of both tide gauge stations taken from the reports at https://www.lacoast.gov/CRMS. CRMS4808 is located in an area with emergent vegetation, and CRMS0479 is located in open water.

approach can be found in more recent algorithms, such as CorPhU [15], where unwrapping error regions are associated with the neighboring larger ones. While this strategy has proven to be very effective for solid-earth applications (e.g., volcano monitoring), it is not sufficient for highly dynamic regions with a mixture of large and small connected components that may show drastic surface changes between them and may also present unwrapping errors, such as in the deltaic wetlands.

The correction [13] depends on accurately defined connected components. However, deltaic wetlands are comprised of numerous islands that often are separated by narrow vegetated channels that can be coherent in the interferograms and, thus, mistakenly grouped into a single connected component by the unwrapping algorithm. Bridging two or more islands with different unwrapping errors may result in erroneous estimations with a significant impact on the correction process. In contrast, our algorithm ensures the best possible separation between connected components by taking advantage of the C_a mask, correcting only for isolated components that require correction to avoid error propagation, and separating the connected components that may have been mistakenly grouped together by the unwrapping algorithm. A similar situation applies to corrections in the time domain (phase closure), for which correct connected component delimitation is also necessary to properly correct phase unwrapping errors. Added to that, the phase closure correction method [13] uses all available interferograms in an L1-norm regularized least-squares optimization to determine the correct number of phase cycles needed to achieve consistency among the available interferogram triplets. For the deltaic wetlands, the approach in [13] is able to improve by 7% and 12% after bridging is applied (see Table I). This is mainly due to the particular characteristics of the dataset used for determining water level change during a

tidal cycle, for which a few images are acquired very rapidly and have very high rates of phase change between consecutive acquisitions. In this case, an iterative approach starting with the shortest temporal baseline interferograms and then growing the interferometric network (NN, NN+1, NN+2, . . .) allowed us to effectively correct persistent unwrapping errors among interferograms. We anticipate this algorithm to work well in other similar cases where there are high rates of phase change.

VI. Conclusion

We find that the enhanced algorithm to correct unwrapping errors substantially improves correct retrieval of water level change from rapid repeat pass SAR acquisitions. Results from our correction algorithm show a 30% improvement in the number of high temporal coherence pixels from the original interferograms for a set of NN, NN + 1, and NN + 2 interferometric pairs. InSAR-derived time-series results and tide-gauge comparison showed good agreement with RMSE values as low as 0.67 cm and up to 4 cm for the worst case. Due to the highly coherent UAVSAR acquisitions, we were able to capture water level change patterns throughout the Wax Lake and Atchafalaya deltas at both high temporal and spatial resolution. These unique observations provide a relevant resource for modeling tidal water flow and sediment transport and deposition in wetlands.

As a whole, the unwrapping correction algorithm proved to be an essential tool to derive valid InSAR estimates of water level change. We note that some intrinsic problems are inherent to the proposed approach, e.g., if there are uncorrected unwrapping errors in the NN interferograms, considered as reliable, they may be passed to the next set of the interferogram to be corrected. This suggests that, for future UAVSAR acquisitions or similar rapid repeat imaging in these settings with rapid water level change, a shorter time span between repeated passes should be considered for periods of high water level change to avoid steep phase gradients that can increase the chances of uncorrected unwrapping errors in the NN pairs. Furthermore, if water level gauges are used for validation or for phase ramp corrections, then care should be taken with their location so that they measure the same water level as InSAR, which requires emergent flooded vegetation. Even though the examples presented here are focused on wetland applications, the algorithm can be used for many other InSAR applications where high spatial gradients or spatially isolated coherent areas are present.

Acknowledgment

This work was performed at the Jet Propulsion Laboratory, California Institute of Technology, under contract with the National Aeronautics and Space Administration (NASA). The NASA Delta-X project is funded by the Science Mission Directorate's Earth Science Division through the Earth Venture Suborbital-3 Program NNH17ZDA001N-EVS3.

References

[1] N. D. Ward *et al.*, "Representing the function and sensitivity of coastal interfaces in Earth system models," *Nature Commun.*, vol. 11, no. 1, pp. 1–14, Dec. 2020, doi: 10.1038/s41467-020-16236-2.

[2] D. Massonnet and K. L. Feigl, "Radar interferometry and its application to changes in the Earth's surface," *Rev. Geophys.*, vol. 36, no. 4, pp. 441–500, Nov. 1998.

[3] R. Bürgmann, P. A. Rosen, and E. J. Fielding, "Synthetic aperture radar interferometry to measure Earth's surface topography and its deformation," *Annu. Rev. Earth Planetary Sci.*, vol. 28, no. 1, pp. 169–209, 2000. [Online]. Available: http://www.annualreviews.org/doi/abs/10.1146/annurev.earth.28.1.169

[4] P. A. Rosen *et al.*, "Synthetic aperture radar interferometry," *Proc. IEEE*, vol. 88, no. 3, pp. 333–382, Mar. 2000.

[5] D. E. Alsdorf, J. M. Melack, T. Dunne, L. A. K. Mertes, L. L. Hess, and L. C. L. Smith, "Interferometric radar measurements of water level changes on the Amazon flood plain," *Nature*, vol. 404, pp. 174–177, Mar. 2000.

[6] Z. Lu, M. Crane, O.-I. Kwoun, C. Wells, C. Swarzenski, and R. Rykhus, "C-band radar observes water level change in swamp forests," *EOS, Trans. Amer. Geophys. Union*, vol. 86, no. 14, pp. 141–144, 2005.

[7] S. Wdowinski, S.-W. Kim, F. Amelung, and T. H. Dixon, "Wetland InSAR: A new space-based hydrological monitoring tool of wetlands surface water level changes," in *Proc. GlobWetland Symp. Proc.*, 2006, p. 1.

[8] T. Oliver-Cabrera and S. Wdowinski, "InSAR-based mapping of tidal inundation extent and amplitude in Louisiana coastal wetlands," *Remote Sens.*, vol. 8, no. 5, p. 393, May 2016. [Online]. Available: http://www.mdpi.com/2072-4292/8/5/393

[9] F. Jaramillo *et al.*, "Assessment of hydrologic connectivity in an ungauged wetland with InSAR observations," *Environ. Res. Lett.*, vol. 13, no. 2, Feb. 2018, Art. no. 024003.

[10] H. Liao, S. Wdowinski, and S. Li, "Regional-scale hydrological monitoring of wetlands with Sentinel-1 InSAR observations: Case study of the South Florida Everglades," *Remote Sens. Environ.*, vol. 251, Dec. 2020, Art. no. 112051, doi: 10.1016/j.rse.2020.112051.

[11] M. Dabboor and B. Brisco, "Wetland monitoring using synthetic aperture radar imagery," in *Wetlands Management-Assessing Risk Sustainable Solutions*, D. Gökçe, Ed. London, U.K.: IntechOpen, 2018, ch. 5, pp. 61–84.

[12] J. Biggs, T. Wright, Z. Lu, and B. Parsons, "Multi-interferogram method for measuring interseismic deformation: Denali fault, Alaska," *Geophys. J. Int.*, vol. 170, no. 3, pp. 1165–1179, 2007.

[13] Z. Yunjun, H. Fattahi, and F. Amelung, "Small baseline InSAR time series analysis: Unwrapping error correction and noise reduction," *Comput. Geosci.*, vol. 133, Dec. 2019, Art. no. 104331, doi: 10.1016/j.cageo.2019.104331.

[14] A. Pepe, "The correction of phase unwrapping errors in sequences of multi-temporal differential SAR interferograms," in *Proc. IEEE Int. Geosci. Remote Sens. Symp.*, Sep. 2020, pp. 818–821.

[15] A. Benoit, B. Pinel-Puysségur, R. Jolivet, and C. Lasserre, "CorPhU: An algorithm based on phase closure for the correction of unwrapping errors in SAR interferometry," *Geophys. J. Int.*, vol. 221, no. 3, pp. 1959–1970, Jun. 2020.

[16] Z.-F. Ma, M. Jiang, M. Khoshmanesh, and X. Cheng, "Time series phase unwrapping based on graph theory and compressed sensing," *IEEE Trans. Geosci. Remote Sens.*, early access, Mar. 26, 2021, doi: 10.1109/TGRS.2021.3066784.

[17] M. Manunta and Y. Muhammad, "A novel algorithm based on compressive sensing to mitigate phase unwrapping errors in multitemporal DInSAR approaches," *IEEE Trans. Geosci. Remote Sens.*, early access, May 25, 2021, doi: 10.1109/TGRS.2021.3079158.

[18] M. Costantini, F. Malvarosa, and F. Minati, "A general formulation for redundant integration of finite differences and phase unwrapping on a sparse multidimensional domain," *IEEE Trans. Geosci. Remote Sens.*, vol. 50, no. 3, pp. 758–768, Mar. 2012.

[19] J.-W. Kim *et al.*, "Integrated analysis of PALSAR/Radarsat-1 InSAR and ENVISAT altimeter data for mapping of absolute water level changes in Louisiana wetlands," *Remote Sens. Environ.*, vol. 113, no. 11, pp. 2356–2365, Nov. 2009, doi: 10.1016/j.rse.2009.06.014.

[20] Z. Lu and O. I. Kwoun, "Radarsat-1 and ERS InSAR analysis over southeastern coastal Louisiana: Implications for mapping water-level changes beneath swamp forests," *IEEE Trans. Geosci. Remote Sens.*, vol. 46, no. 8, pp. 2167–2184, Aug. 2008.

[21] B. R. Couvillion, H. Beck, D. Schoolmaster, and M. Fischer, "Land area change in coastal Louisiana (1932 to 2016)," U.S. Geological Survey Sci. Invest., Menlo Park, CA, USA, Tech. Rep. Map 3381, 16 p. pamphlet, 2017, p. 16, doi: 10.3133/sim3381.

[22] J. Barras *et al.*, "Historical and projected coastal Louisiana land changes: 1978-2050," USGS, New York, NY, USA, Tech. Rep. 03–334, 2003, p. 39. [Online]. Available: http://www.louisianaspeaks-parishplans.org/projectattachments/001246/NewHistoricalland.pdf

[23] B. R. Couvillion *et al.*, "Land area change in coastal Louisiana from 1932 to 2010," U.S. Geological Surv. Sci. Invest., Menlo Park, CA, USA, Tech. Rep. Map 3164, scale 1:265,000, 12 p. pamphlet, 2011, p. 12.
[24] P. A. Rosen, E. Gurrola, G. F. Sacco, and H. Zebker, "The InSAR scientific computing environment," in *Proc. Eur. Conf. Synth. Aperture Radar (EUSAR)*, Apr. 2012, pp. 730–733.
[25] C. W. Chen and H. A. Zebker, "Network approaches to two-dimensional phase unwrapping: Intractability and two new algorithms: Erratum," *J. Opt. Soc. Amer. A, Opt. Image Sci.*, vol. 18, no. 5, p. 1192, 2001.
[26] G. F. Carballo and P. W. Fieguth, "Hierarchical network flow phase unwrapping," *IEEE Trans. Geosci. Remote Sens.*, vol. 40, no. 8, pp. 1695–1708, Aug. 2002.
[27] C. W. Chen and H. A. Zebker, "Phase unwrapping for large SAR interferograms: Statistical segmentation and generalized network models," *IEEE Trans. Geosci. Remote Sens.*, vol. 40, no. 8, pp. 1709–1719, Aug. 2002.
[28] R. Jolivet, R. Grandin, C. Lasserre, M. P. Doin, and G. Peltzer, "Systematic InSAR tropospheric phase delay corrections from global meteorological reanalysis data," *Geophys. Res. Lett.*, vol. 38, no. 17, pp. 1–6, 2011.
[29] R. Jolivet *et al.*, "Improving InSAR geodesy using global atmospheric models," *J. Geophys. Res., Solid Earth*, vol. 119, no. 3, pp. 2324–2341, 2014.
[30] C. Yu, N. T. Penna, and Z. Li, "Generation of real-time mode high-resolution water vapor fields from GPS observations," *J. Geophys. Res., Atmos.*, vol. 122, no. 3, pp. 2008–2025, 2017.
[31] C. Yu, Z. Li, N. T. Penna, and P. Crippa, "Generic atmospheric correction model for interferometric synthetic aperture radar observations," *J. Geophys. Res., Solid Earth* vol. 123, no. 10, pp. 9202–9222, Oct. 2018.
[32] C. Yu, Z. Li, and N. T. Penna, "Interferometric synthetic aperture radar atmospheric correction using a GPS-based iterative tropospheric decomposition model," *Remote Sens. Environ.*, vol. 204, pp. 109–121, Jan. 2018, doi: 10.1016/j.rse.2017.10.038.
[33] P. Berardino *et al.*, "A new algorithm for monitoring localized deformation phenomena based on small baseline differential SAR interferograms," in *Proc. IEEE Int. Geosci. Remote Sens. Symp.*, Jun. 2002, vol. 2, no. 11, pp. 2375–2383. [Online]. Available: http://ieeexplore.ieee.org/document/1025900/
[34] A. Pepe and R. Lanari, "On the extension of the minimum cost flow algorithm for phase unwrapping of multitemporal differential SAR interferograms," *IEEE Trans. Geosci. Remote Sens.*, vol. 44, no. 9, pp. 2374–2383, Sep. 2006.

Talib Oliver-Cabrera received the B.S. degree in geomatics engineering from the National Autonomous University of Mexico, Mexico, Mexico City, in 2010, and the Ph.D. degree in marine geology and geophysics from the University of Miami, Miami, FL, USA, in 2018.

He is currently a Post-Doctoral Fellow with the Jet Propulsion Laboratory (JPL), California Institute of Technology, Pasadena, CA, USA. His work at JPL is focused on the processing of synthetic aperture radar images acquired by the uninhabited aerial vehicle synthetic aperture radar (UAVSAR) for the Delta-X mission. His research interests include SAR processing, algorithm development, radar interferometry, and interferometric synthetic aperture radar (InSAR) applications for wetland and hazards monitoring.

Cathleen E. Jones (Member, IEEE) received the B.S. degree in physics from Texas A&M University, College Station, TX, USA, in 1982, and the Ph.D. degree in physics from the California Institute of Technology, Pasadena, CA, USA, in 1991.

She is currently a Radar Scientist with the Jet Propulsion Laboratory, California Institute of Technology. She is also the Applications Lead of the NISAR Science Team. Her research is focused on using synthetic aperture radar for studying natural and man-made hazards and includes the development of methods for tracking and characterizing oil slicks, measuring water level change and subsidence in deltas, and monitoring critical infrastructure.

Zhang Yunjun received the B.Eng. degree in remote sensing from Wuhan University, Wuhan, China, in 2011, the M.Sc. degree in geodesy from the University of Chinese Academy of Sciences, Beijing, China, in 2014, and the Ph.D. degree in geophysics from the University of Miami, Miami, FL, USA, in 2019.

He has been a Post-Doctoral Scholar Research Associate in geophysics with the California Institute of Technology, Pasadena, CA, USA, since November 2019. His research interests include algorithm and tools development for interferometric synthetic aperture radar (InSAR) time-series analysis and solid earth processes associated with active volcanism and activate tectonics.

Marc Simard received the B.Sc. degree (Hons.) in physics with a focus on astrophysics from Queen's University, Kingston, ON, Canada, in 1992, and the M.Sc. degree in physics and the Ph.D. degree in geomatics from the Université Laval, Quebec, QC, Canada, in 1994 and 1998, respectively.

He is currently a Principal Scientist with NASA's Jet Propulsion Laboratory, Pasadena, CA, USA. His research focuses on the development and use of radar remote sensing technology to understand the role of large-scale climatic and hydrogeomorphic processes on vegetation structure, with a particular emphasis on coastal regions. He has recently led the development of new multi-instrument airborne remote sensing techniques to measure the hydrology and sediment transport in coastal ecosystems. These techniques led to the new Earth Venture Suborbital Delta-X Mission, which will improve the modeling of soil accumulation rates in coastal wetlands. In parallel, he is working on the development of new spaceborne missions, such as NISAR and SWOT, to monitor vegetation and hydrology of forested and coastal landscapes.

Dr. Simard is also a member of the Surface Water and Ocean Topography Mission, a spaceborne Ka-band radar interferometer, planned for launch in 2022. He is also an Active Member of the International Blue Carbon Working Group.